ADVANCED ENERGY MATERIALS

Supporting Information

for *Adv. Energy Mater.,* DOI: 10.1002/aenm.202102618

Enabling 4C Fast Charging of Lithium-Ion Batteries by Coating Graphite with a Solid-State Electrolyte

*Eric Kazyak, Kuan-Hung Chen, Yuxin Chen, Tae H. Cho, and Neil P. Dasgupta**

WILEY-VCH

Supporting Information

Enabling 4C Fast Charging of Lithium-ion Batteries by Coating Graphite with a Solid-State Electrolyte

*Eric Kazyak[‡], Kuan-Hung Chen[‡], Yuxin Chen, Tae H. Cho, Neil P. Dasgupta**

Table S1. Review of literature on modified graphite electrodes for improved rate performance or fast-charging.

Approach	Electrolyte	Graphite Loading (mAh/cm^2)	Cell Format (electrode size)	Temp. °C	Cycling C-rate	Cycles/retention (control)	Cycles/retention (Modified)	Reference
3D structuring								
Laser-patterning	1 M $LiPF_6$ in 3:7 EC:EMC with 2% VC	2.9/3.2	Multi-layer Pouch cell (70 cm2)	30°C	4C,6C	4C - 100x/69%, 6C - 100x/59%	4C - 100x/97%, 600x/91%; 6C - 100x/93%, 600x/86%	[1]
Laser Patterning	1 M $LiPF_6$ in 2:1:7 EC:PC:EMC	1.15,4,5.5	Swagelok (9.5 mm Ø)	N/A	N/A	Half Cells Only		[2]
KOH etching	1 M $LiPF_6$ in 3:7 EC:DEC	1.62	?	?	3C, 6C	3C - 100x/85%, 6C - 100x/50%	3C - 100x/93%; 6C - 100x/74%	[3]
KOH etching	1.15 M $LiPF_6$ in 3:3:4 EC:DMC:EMC	?	2032 Coin	?	2.5C	2.5C - 100x/47%	2.5C - 100x/94.5%	[4]
Dual-scale porosity	1.3 M $LiPF_6$ in blend of alkyl carbonates	?	Swagelok (5 mm x 5 mm)	N/A	N/A	No fast-charge cycling		[5]
Freeze-drying	1 M $LiPF_6$ in 1:1 EC:DEC with 10% FEC	?	2032 Coin	N/A	N/A	Half Cells Only		[6]
Edge plane activation	1.3 M $LiPF_6$ in 3:5:2 EC:EMC:DEC	3.5	Pouch (?)	?	3C	3C - 50x/40%	3C - 50x/68%	[7]
Coatings								
ALD TiO_2	1 M $LiPF_6$ in 3:1:4:2 EC:PC:EMC:DMC	6	2032 Coin	N/A	N/A	Half Cells only		[8]
Polymer	1M $LiPF_6$ in 1:1 EC:EMC	0.76	2032 Coin	N/A	N/A	No fast-charge cycling		[9]
Solution-based TiO_2	1M $LiPF_6$ in 3:7 EC:EMC	0.84	Single Layer Pouch (12 cm2)	RT	5C	5C - 100x/98%	5C - 100x/97%	[10]
Al_2O_3	1M $LiPF_6$ in 3:7 EC:EMC	0.84	2032 Coin	RT	1.1C	1.1C - 100x/91%	1.1C - 100x/94%	[11]
Sol-gel Al_2O_3	1M $LiPF_6$ in 1:1 EC:EMC	?	2016 Coin	N/A	N/A	Half Cells only		[12]
Sputtered Ni	1 M $LiPF_6$ in 3:7 EC:DMC	2.5	Single Layer Pouch (23.7 cm2)	RT	6C	6C - 100x/86%, 300x/79%	6C - 100x/90%, 300x/85%	[13]
Sputtered Cu	1M $LiPF_6$ in 3:7 EC:DMC with 2% VC	3	Single Layer Pouch (?)	30°C	6C	6C - 100x/82%, 500x/71%	6C - 100x/89%, 500x/79%	[14]
Nano-diamond	1.2M $LiPF_6$ in 3:7 EC:EMC	3.1	2032 Coin	27°C	N/A	Half Cells only		[15]
LTO	1M $LiPF_6$ in 1:1 EC:DMC	8	2032 Coin	N/A	N/A	Half Cells only		[16]
Cu	1 M $LiPF_6$ 2:2:1 EC:DEC:PC	?	?	N/A	N/A	Half Cells only		[17]
Carbon	1M $LiPF_6$ in 1:1 EC:DMC (w/w) with 2 wt.% FEC	2.4-2.7	2032 Coin	N/A	N/A	Half Cells only		[18]
Carbon	1 M $LiPF_6$ in 3:7 EC:EMC	0.48	Pouch Cell (?)	RT	2C, 3C	2C - 500x/89%; 3C - 500x/85%	2C - 500x/90%; 3C - 500x/87%	[19]
ALD LBCO	1M $LiPF_6$ in 3:7 EC:EMC with 2% VC	3.2	Single-layer Pouch (70 cm2)	30°C	4C	4C - 100x/64%, 500x/60%	4C - 100x/87%, 500x/80%	This work

Thickness-dependent cycling performance of coin cells:
The 250x and 500x LBCO coated cells exhibited significantly improved rate capability and capacity retention compared to the control (Figure S). The LBCO 50x cell was initially better than the control, but during extended cycling, eventually converged with the controls. This is consistent with the observation in Figure 2a-b that the 50x coating was not sufficient to passivate the electrode surface. Furthermore, the heated control exhibited similar cycling performance to the unheated controls. Therefore, the observed differences in behavior are attributed to the coating itself, rather than the processing conditions.

Additional EIS fitting details:

The circuit elements used to fit graphite electrodes typically include: 1) a resistance (R_{series}) associated with the ohmic drop; 2) a resistance ($R_{P\text{-}CC}$) associated with the contact between the graphite particles and between the graphite and the current collector; 3) a resistance (R_{SEI}) associated with ionic transport through the SEI; 4) a resistance (R_{CT}) associated with charge transfer processes; and 5) a diffusion element associated with solid-state diffusion within the graphite particles. $R_{P\text{-}CC}$, R_{SEI}, and R_{CT} each have a capacitance associated with them. Constant phase elements were used for fitting $R_{P\text{-}CC}$ and R_{CT} to account for the suppressed semi-circles that are observed. In addition, a Havriliak-Negami (HN) term[20] was used in conjunction with the SEI resistance to capture the asymmetry of the SEI impedance feature in the spectra. This asymmetry has been observed previously,[21] and is generally accounted for by incorporating either a transmission line model or an HN element. It arises due to the combination of ionic transport through the SEI layer and the electrochemical reactions occurring at the surface of the SEI.

Electrode porosity
The porosity of the electrode is calculated via measuring the mass loading and the thickness of the electrode (Eq. x).

$$\epsilon = m \times \left(\frac{\varepsilon_{active}}{\rho_{active}} + \frac{\varepsilon_{C65}}{\rho_{C65}} + \frac{\varepsilon_{binder}}{\rho_{binder}} \right) \times \frac{1}{t} \quad (Eq.x)$$

Where ϵ is the porosity of the electrode; m is the area specific mass loading of the electrode; ε_{active}, ε_{C65}, and ε_{binder} are the weight percentage of the active material, C65 conductive additive and the binder, respectively; ρ_{active}, ρ_{C65}, and ρ_{binder} are the density of the active material, C65 conductive additive and the binder, respectively; and t is the thickness of the electrode.
The porosity of the electrodes was chosen to be around 30%. A low porosity of the electrode is desired because lower porosity can reduce the volume of the battery and the amount of electrolyte, and thus increase the energy density. However, when porosity is lower than 30%, the tortuosity of the electrode dramatically increase, and thus hinders the diffusion of Li^+ in the electrolyte [22].

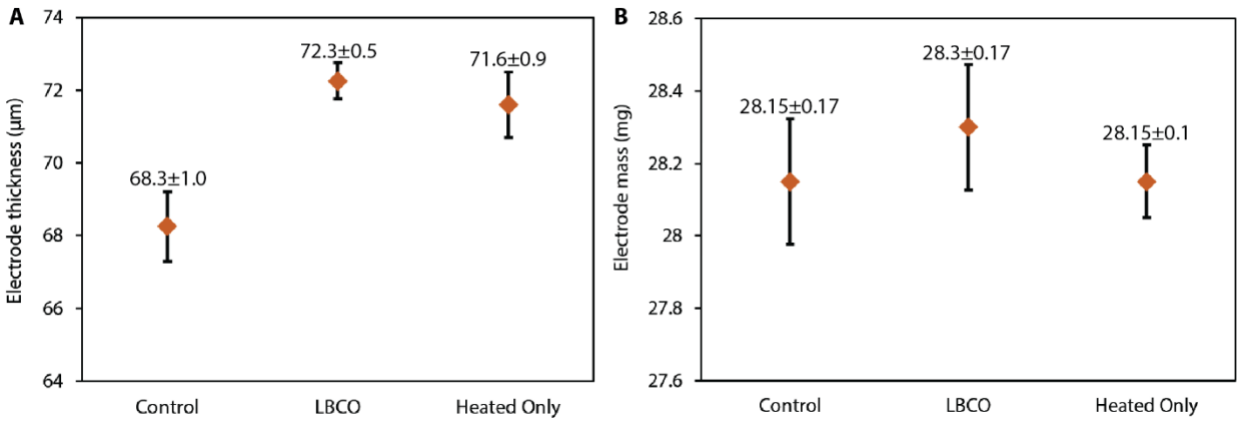

Figure S1. (A) Measured thickness of graphite electrodes after subtracting current collector thickness for control, heated control, and LBCO 250x. (B) Mass of punched electrode pieces for the same 3 treatments. Each mass/thickness measurement was taken on 5 separate areas and averaged. The error bars represent one standard deviation.

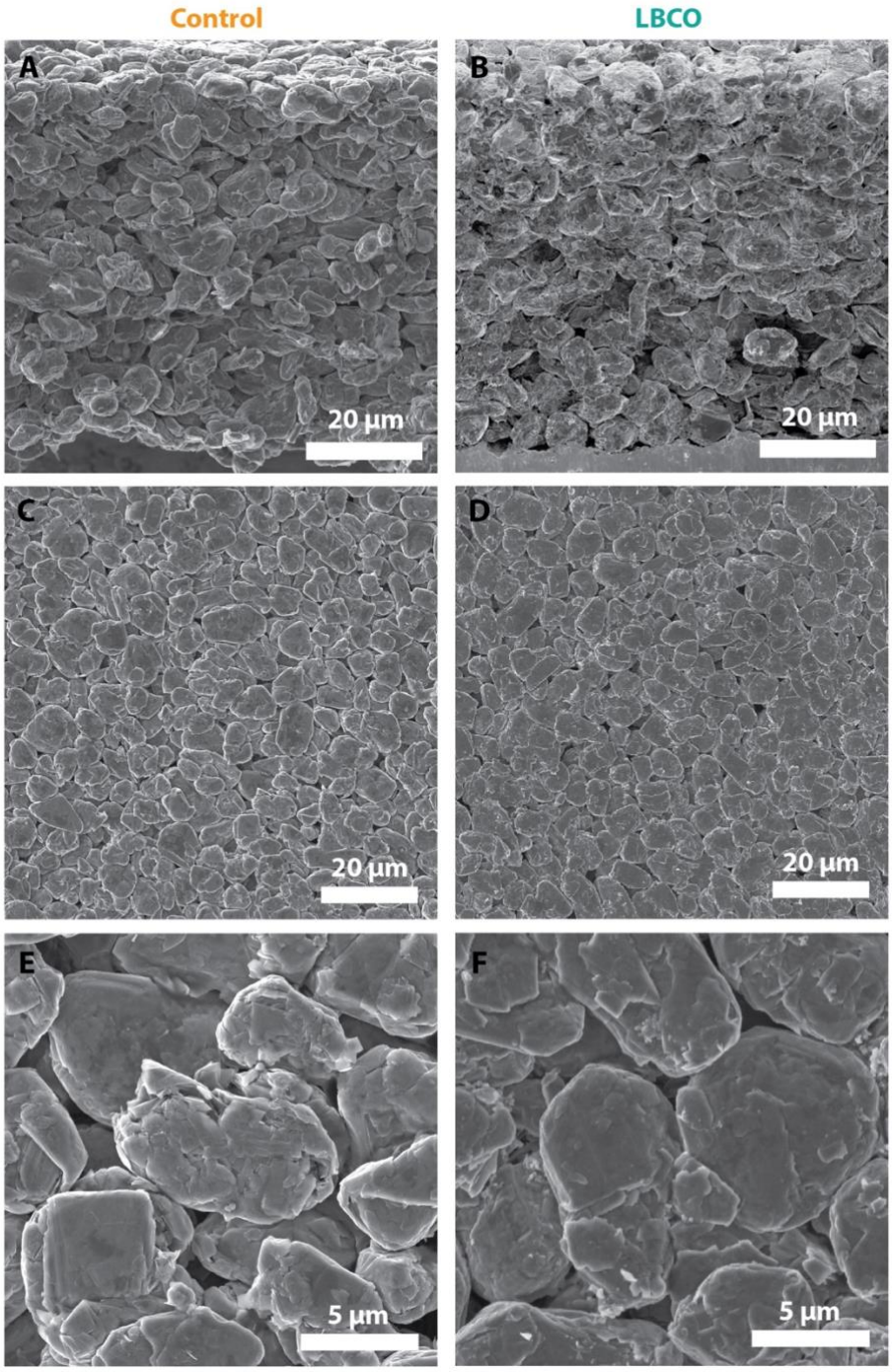

Figure S2. Scanning electron micrographs of graphite electrodes before (A,C,E) and after (B,D,F) coating with ALD LBCO film. Images show that the porosity is not significantly altered due to the conformality of the thin coating.

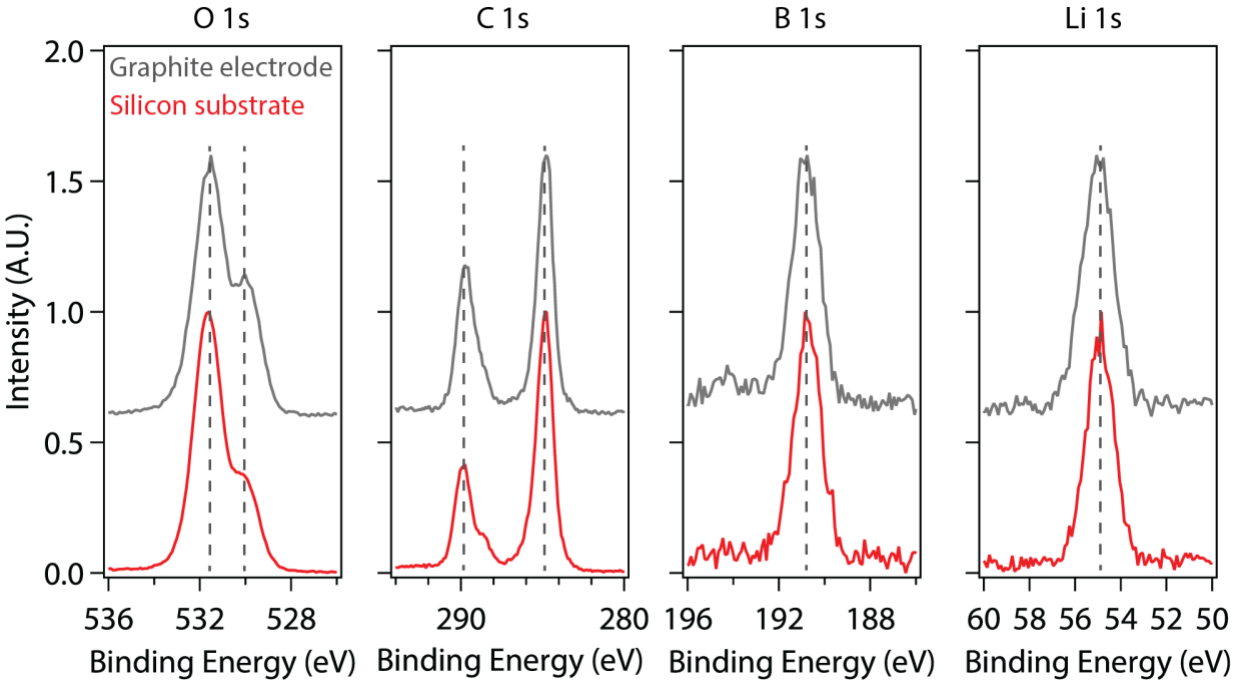

Figure S3. X-ray Photoelectron spectroscopy of LBCO ALD film on graphite and Silicon substrates. Oxygen, Carbon, Boron, and Lithium core scans show similarity of the LBCO deposited on graphite with that on Silicon, which was thoroughly characterized in our previous report.[23]

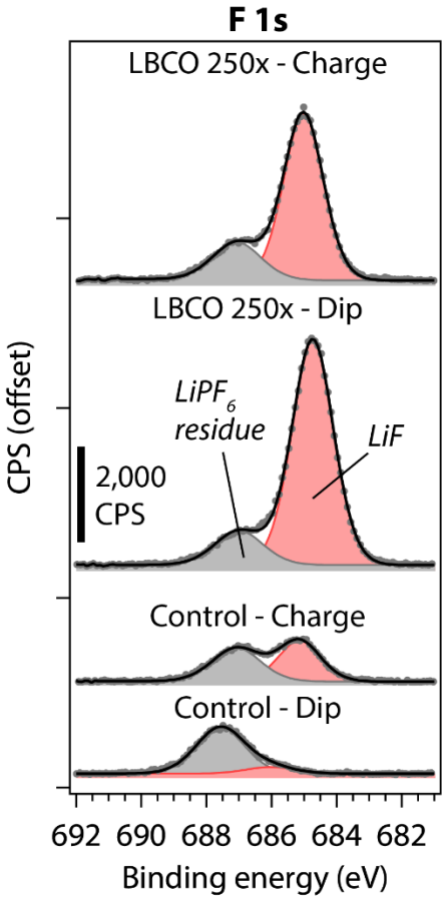

Figure S4. F 1s core scans for control and LBCO 250x electrodes after dipping into electrolyte for 30 min. and after charging to 4.2 V.

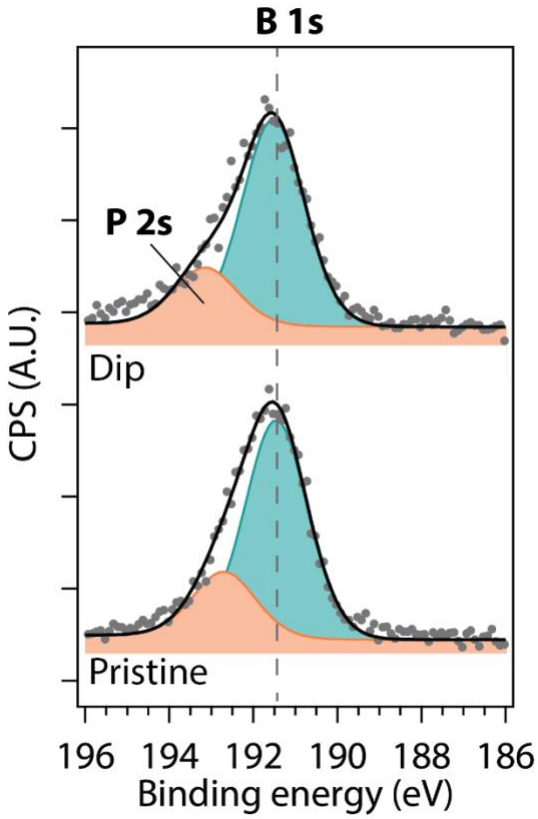

Figure S5. B 1s core scans for LBCO 250x electrodes before (pristine) and after (Dip) dipping in $LiPF_6$-based electrolyte. Both are after 120 s of Ar sputtering, removing surface species. No BE shifts are evident between the two spectra, and the binding energy value for the B 1s of LBCO is consistent with our previous work (191.6 eV). This indicates that the LBCO film remains intact on the graphite surface after dipping.

Table S2. Practical Effective Attenuation Length calculation performed using the NIST Electron Effective Attenuation Length Database for B 1s photoelectrons excited by Al Kα x-rays travelling through a lithium fluoride overlayer. At the selected depth of 1.0 nm, the signal from the underlying film is attenuated to 74.6%, similar to the observed decrease in B 1s signal after immersion of the LBCO-coated graphite in the electrolyte.

Parameter	Value
B 1s Photoelectron kinetic energy	1306 eV
Incident x-ray angle	54°
Asymmetry parameter	2
Assumed overlayer composition	LiF
LBCO layer signal with 1 nm overlayer	74.6 %

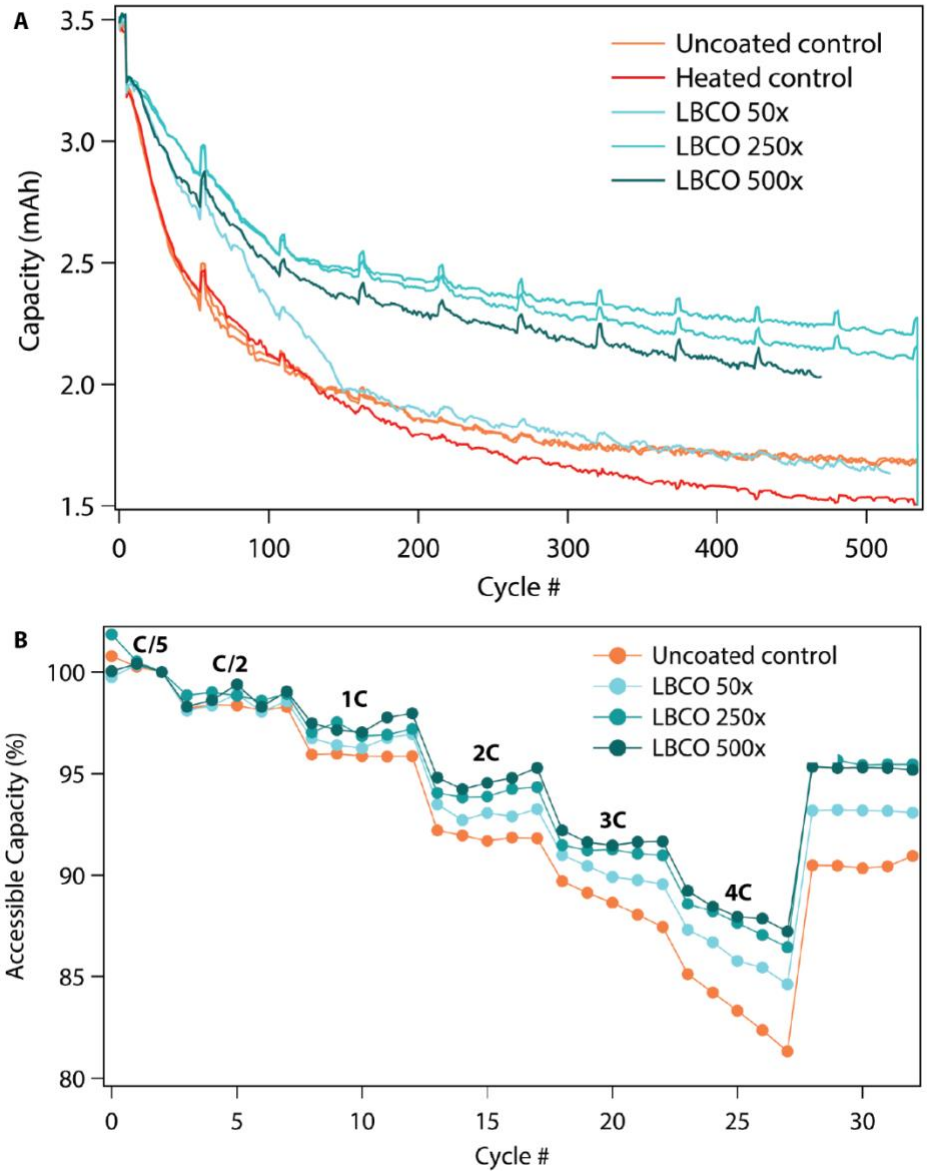

Figure S6. (A) Discharge capacity vs. cycle life for various electrode treatments. (B) Discharge capacity for various LBCO coating thicknesses at increasing charging rates. Cells were discharged at C/2 for all cycles.

	Control	LBCO
Cu foil thickness (µm)	10	
Anode loading (mg/cm^2)	9.40	
Anode porosity (%)	32	
Anode thickness (µm)	65.5	
Separator thickness (µm)	12	
Separator porosity (%)	47	
Cathode loading (mg/cm^2)	16.58	
Cathode porosity (%)	35	
Cathode thickness (µm)	61.5	
Al foil thickness (µm)	15	
Stack mass (mg/cm^2)	37.05	
Total area (cm^2)	69.69	
Stack weight (g)	2.58	
Discharge energy at C/3 (Wh)	0.59	0.59
Stack specific energy (Wh/kg)	228	228

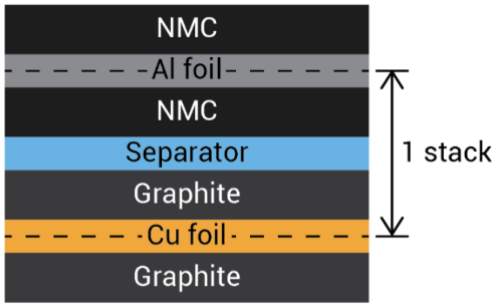

Figure S7. Calculation of stack specific energy density. (left) Table of parameters used in pouch cells. (right) Schematic of the unit cell used for the calculation.

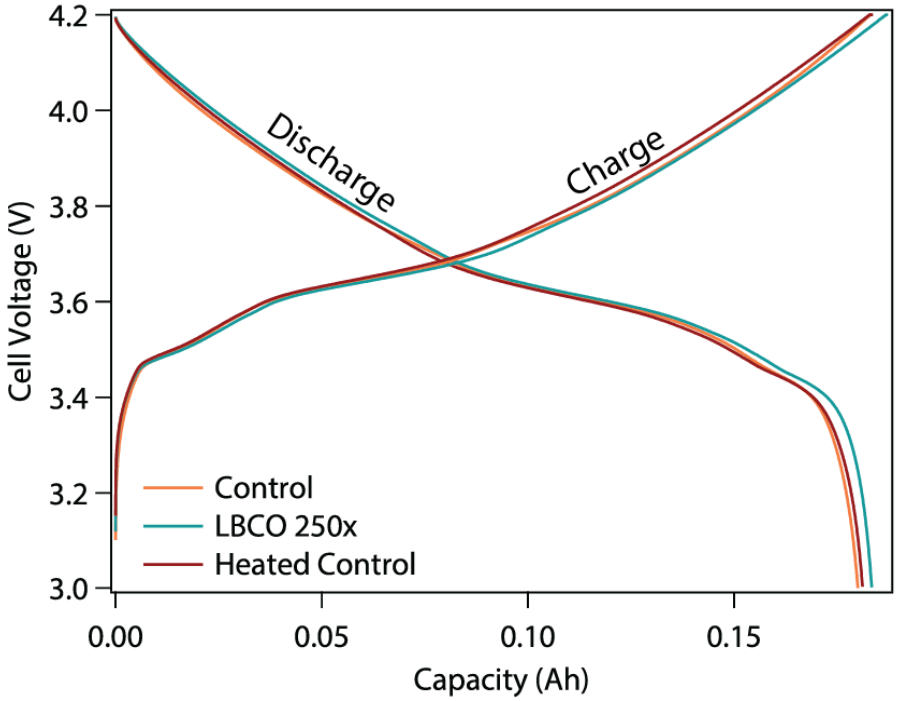

Figure S8. Charge and discharge curves for uncoated control and LBCO 250x pouch cells at C/10 showing similar behavior of both cells at low rates.

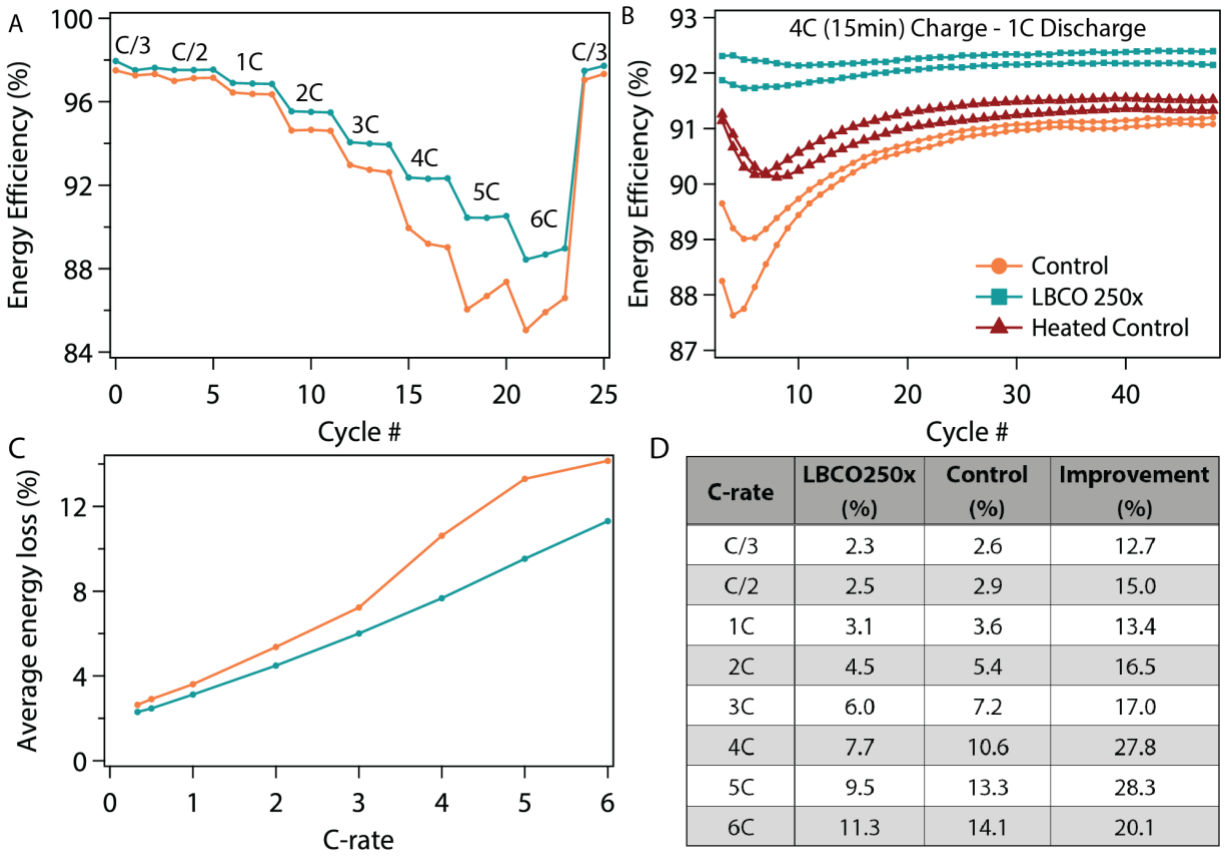

C-rate	LBCO250x (%)	Control (%)	Improvement (%)
C/3	2.3	2.6	12.7
C/2	2.5	2.9	15.0
1C	3.1	3.6	13.4
2C	4.5	5.4	16.5
3C	6.0	7.2	17.0
4C	7.7	10.6	27.8
5C	9.5	13.3	28.3
6C	11.3	14.1	20.1

Figure S9. (A) Energy efficiency (ratio of discharge energy to charge energy) of control and LBCO 250X single layer pouch cells at various C-rates. (B) Energy efficiency of control, heated control, and LBCO 250X single layer pouch cells during first 50 4C (15-min) fast-charge cycles. (C) Average energy loss for the cells in (A) for each C-rate. (D) Table of values from (C) with quantification of the improvement in energy loss for the LBCO 250X cell compared to the control.

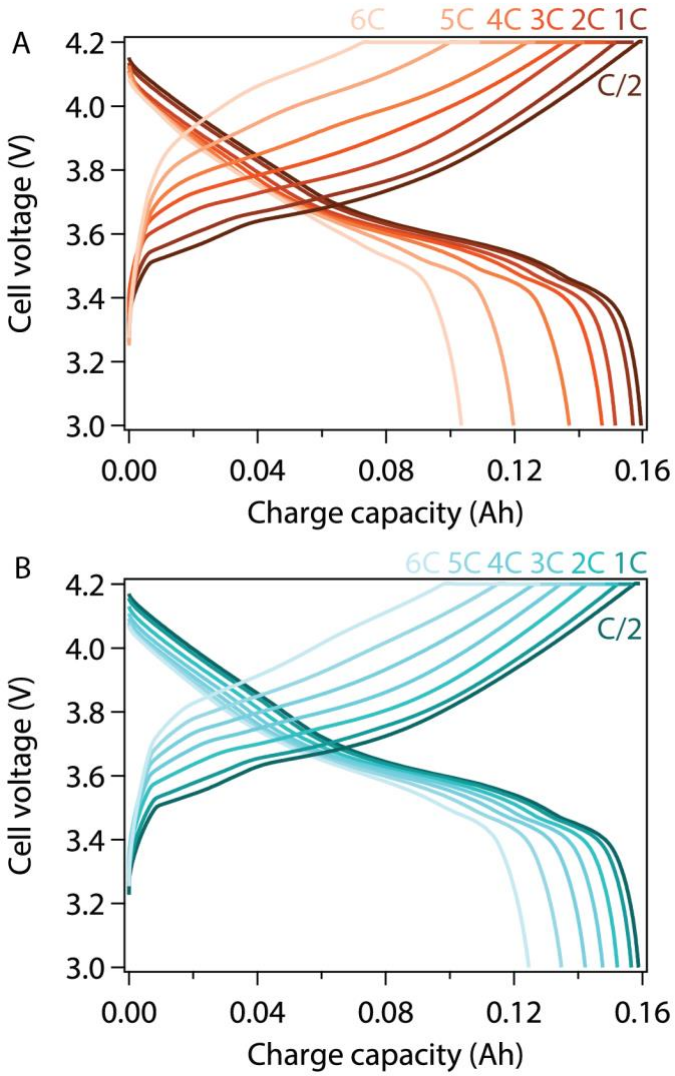

Figure S10. Charge and discharge curves for control (A) and LBCO 250X (B) single layer pouch cells at various C-rates from C/2 to 6C.

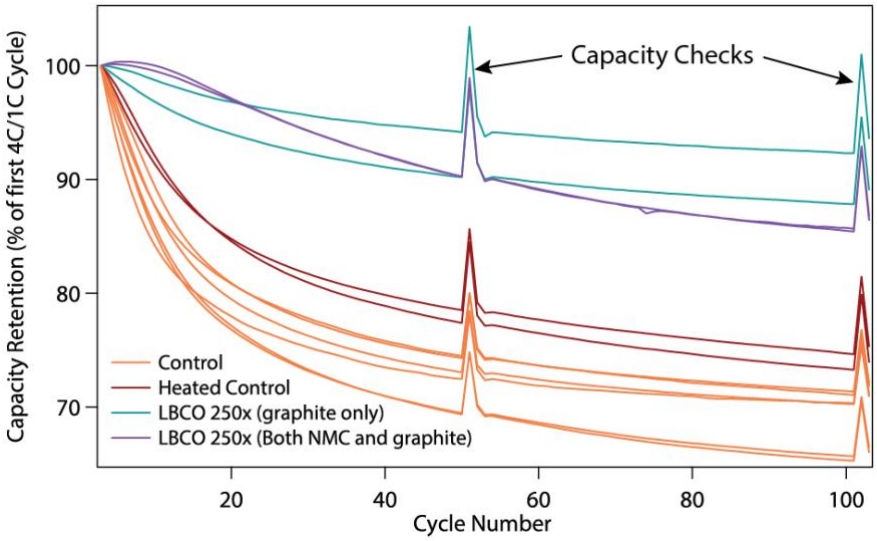

Figure S11. Capacity retention of single-layer pouch cells during cycling with 4C (15 min.) charging and 1C discharging. Capacity values are normalized to the initial fast-charge cycles.

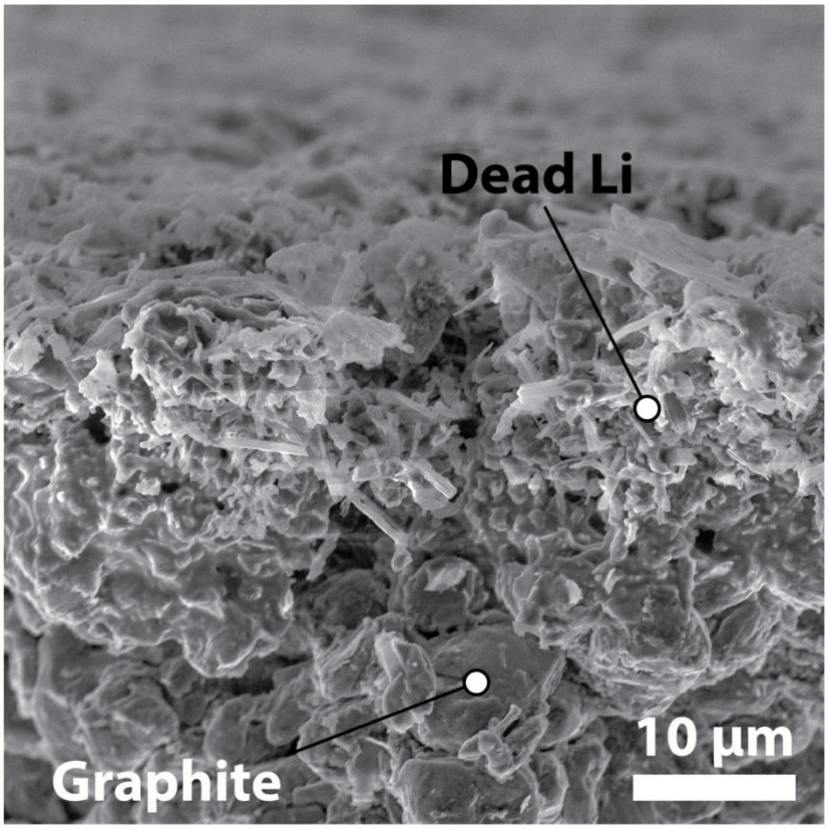

Figure S12. Scanning electron micrograph of control graphite electrode after 100 4C (15-min) fast-charge cycles showing the distinct morphology of the dead Li layer from the graphite particles. This difference was used to identify the dead Li for false-coloring of Figure 4.

Table S3. Fit results for 3-electrode EIS data and fits shown in Figure 5. Area of working electrode was 2.545 cm^2.

Sample Units	**SOC** (mV)	$\mathbf{R_{series}}$ Ω	$\mathbf{R_{P\text{-}CC}}$ Ω	$\mathbf{Q_{P\text{-}CC}}$ F	$\boldsymbol{\alpha_{P\text{-}CC}}$ -	$\mathbf{R_{SEI}}$ Ω	$\mathbf{C_{HN}}$ F	$\boldsymbol{\tau_{HN}}$ s	$\boldsymbol{\alpha_{HN}}$ -	$\boldsymbol{\beta_{HN}}$ -	$\mathbf{R_{CT}}$ Ω	$\mathbf{Q_{CT}}$ F	$\boldsymbol{\alpha_{CT}}$ -	$\mathbf{W_{diff.}}$ $\Omega\text{-}s^{-1/2}$
Control	200	4.12	1.16	1.24E-6	1	7.0	4.83E-4	8.13E-3	0.74	0.68	11.4	1.7E-2	0.85	1.2
Control	120	4.05	1.15	1.22E-6	1	6.8	5.24E-4	9.24E-3	0.68	0.74	1.95	1.9E-2	0.86	0.39
Control	83	3.94	1.11	1.28E-6	1	7.0	5.27E-4	9.14E-3	0.68	0.75	1.67	2.2E-2	0.93	0.48
LBCO 250x	200	3.19	1.31	1.27E-6	1	1.6	2.73E-4	2.07E-3	0.95	0.49	10.2	2.11E-2	0.81	1.57
LBCO 250x	120	3.20	1.32	1.24E-6	1	1.6	3.99E-4	4.30E-3	0.95	0.49	1.17	1.77E-2	0.89	0.50
LBCO 250x	83	3.15	1.29	1.30E-6	1	1.6	4.02E-4	4.25E-3	0.95	0.49	1.62	1.57E-2	0.92	0.52

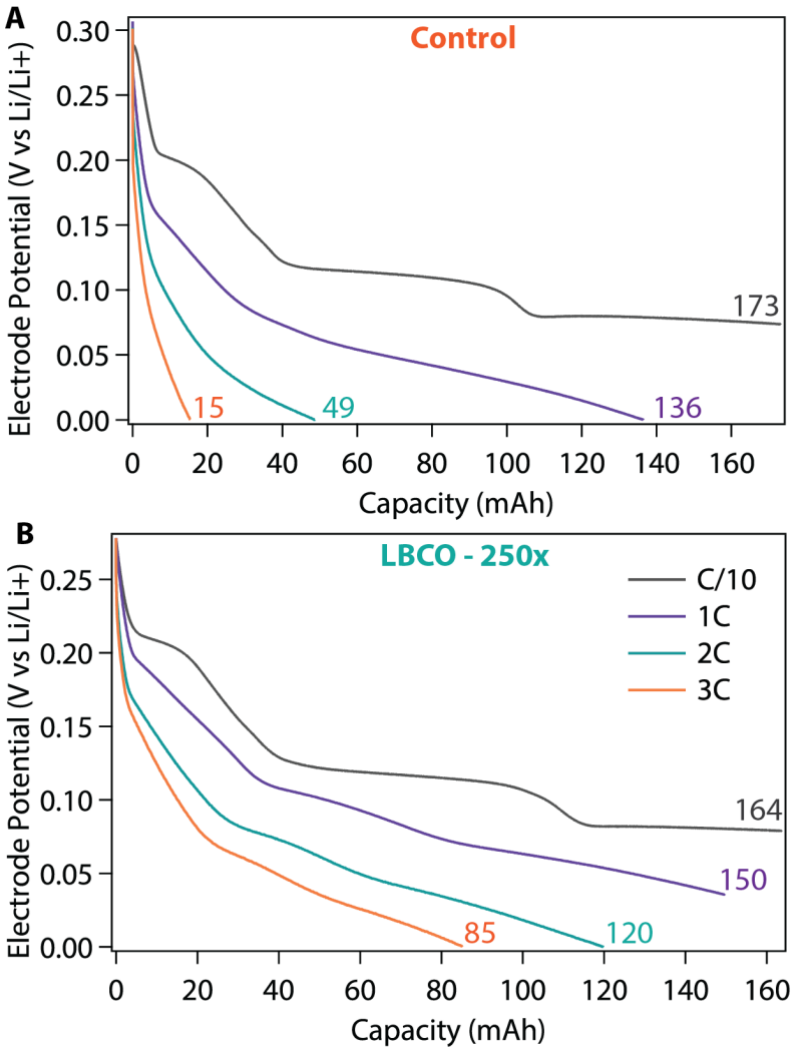

Figure S13. Charging curves at various C-rates from C/10 to 3C for control and LBCO 250X graphite electrodes in a 3-electrode single-layer pouch cell using a lithiated gold-coated microwire reference electrode.

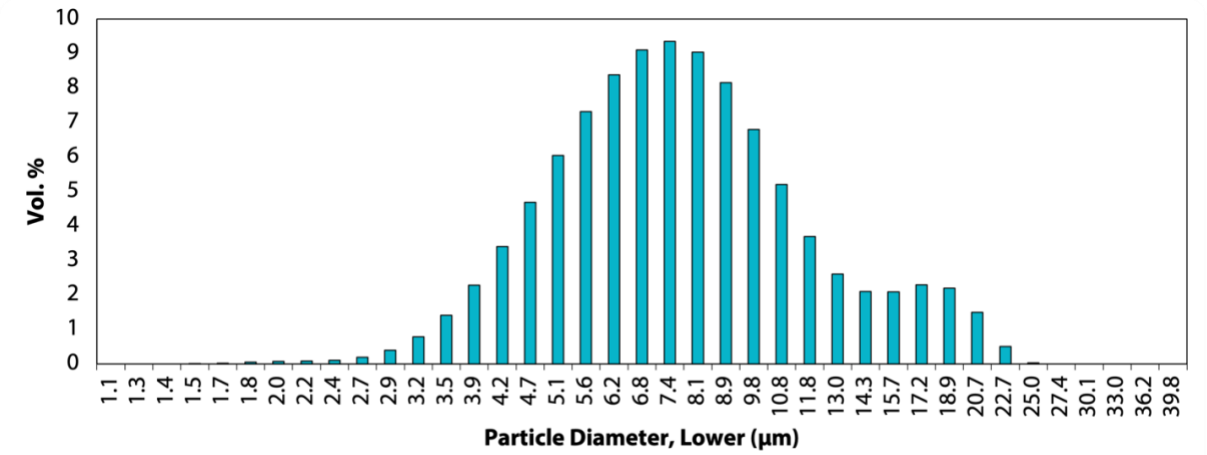

Figure S14. Particle size distribution of natural graphite powder used to fabricate the electrodes used in this work. Distribution was measured using laser diffraction particle size an**alyzer (Beckman Coulter).**

References

[1] K.-H. Chen, M. J. Namkoong, V. Goel, C. Yang, S. Kazemiabnavi, S. M. Mortuza, E. Kazyak, J. Mazumder, K. Thornton, J. Sakamoto, N. P. Dasgupta, *J. Power Sources* **2020**, *471*, 228475.

[2] Y. Kim, A. Drews, R. Chandrasekaran, T. Miller, J. Sakamoto, *Ionics (Kiel).* **2018**, *24*, 2935.

[3] Q. Cheng, R. Yuge, K. Nakahara, N. Tamura, S. Miyamoto, *J. Power Sources* **2015**, *284*, 258.

[4] J. H. Shim, S. Lee, *J. Power Sources* **2016**, *324*, 475.

[5] C.-J. Bae, C. K. Erdonmez, J. W. Halloran, Y.-M. Chiang, *Adv. Mater.* **2013**, *25*, 1254.

[6] D. Dang, Y. Wang, S. Gao, Y. T. Cheng, *Carbon N. Y.* **2020**, *159*, 133.

[7] N. Kim, S. Chae, J. Ma, M. Ko, J. Cho, *Nat. Commun.* **2017**, *8*, 1.

[8] M. L. Lee, C. Y. Su, Y. H. Lin, S. C. Liao, J. M. Chen, T. P. Perng, J. W. Yeh, H. C. Shih, *J. Power Sources* **2013**, *244*, 410.

[9] Q. Shi, S. Heng, Q. Qu, T. Gao, W. Liu, L. Hang, H. Zheng, *J. Mater. Chem. A* **2017**, *5*, 10885.

[10] D. S. Kim, D. J. Chung, J. Bae, G. Jeong, H. Kim, *Electrochim. Acta* **2017**, *258*, 336.

[11] D. S. Kim, Y. E. Kim, H. Kim, *J. Power Sources* **2019**, *422*, 18.

[12] T. Feng, Y. Xu, Z. Zhang, X. Du, X. Sun, L. Xiong, R. Rodriguez, R. Holze, *ACS Appl. Mater. Interfaces* **2016**, *8*, 6512.

[13] K. R. Tallman, B. Zhang, L. Wang, S. Yan, K. Thompson, X. Tong, J. Thieme, A. Kiss, A. C. Marschilok, K. J. Takeuchi, D. C. Bock, E. S. Takeuchi, *ACS Appl. Mater. Interfaces* **2019**, *11*, 46864.

[14] K. R. Tallman, S. Yan, C. D. Quilty, A. Abraham, A. H. McCarthy, A. C. Marschilok, K. J. Takeuchi, E. S. Takeuchi, D. C. Bock, *J. Electrochem. Soc.* **2020**, *167*, 160503.

[15] Y. W. Cheng, R. K. Pandey, Y. C. Li, C. H. Chen, B. L. Peng, J. H. Huang, Y. X. Chen, C. P. Liu, *Nano Energy* **2020**, *74*, 104811.

[16] M. L. Lee, Y. H. Li, S. C. Liao, J. M. Chen, J. W. Yeh, H. C. Shih, *Appl. Surf. Sci.* **2012**, *258*, 5938.

[17] K. Guo, Q. Pan, L. Wang, S. Fang, *J. Appl. Electrochem.* **2002**, *32*, 679.

[18] V. Sharova, A. Moretti, G. Giffin, D. Carvalho, S. Passerini, *C* **2017**, *3*, 22.

[19] X. Liao, Z. Ding, Z. Yin, *Ionics (Kiel).* **2020**, *26*, 5367.

[20] S. Havriliak, S. Negami, *Polymer (Guildf).* **1967**, *8*, 161.

[21] J. Illig, M. Ender, A. Weber, E. Ivers-Tiffée, *J. Power Sources* **2015**, *282*, 335.

[22] L. Shen, Z. Chen, *Chem. Eng. Sci.* **2007**, *62*, 3748.

[23] E. Kazyak, K.-H. Chen, A. L. Davis, S. Yu, A. J. Sanchez, J. Lasso, A. R. Bielinski, T. Thompson, J. Sakamoto, D. J. Siegel, N. P. Dasgupta, *J. Mater. Chem. A* **2018**, *6*, 19425.